Appl. Phys. A (2017) 123:224
DOI 10.1007/s00339-017-0850-4

Applied Physics A
Materials Science & Processing

CrossMark

Electrical and photoresponse properties of vacuum deposited Si/Al:ZnSe and Bi:ZnTe/Al:ZnSe photodiodes

Gowrish K. Rao[1]

Received: 26 October 2016 / Accepted: 12 February 2017 / Published online: 8 March 2017
© Springer-Verlag Berlin Heidelberg 2017

Abstract The paper reports fabrication and characterization of Bi:ZnTe/Al:ZnSe and Si/Al:ZnSe thin film photodiodes. The characteristics of the devices were studied under dark and illuminated conditions. The normalized spectral response, speed of photoresponse and variation of photocurrent with power density were studied in detail. Many vital parameters, such as diode ideality factor, barrier height, the thickness of the depletion region, trap depth, rise and decay times of photocurrent, were determined. Conduction mechanism in the photodiodes is discussed with the help of widely accepted theoretical models.

1 Introduction

Photodiodes based on II–VI compound semiconductors can yield high quantum efficiency due to their direct bandgap [1–7]. Since these materials have a wide band gap, they are ideally suitable for photodiodes in the UV-Visible-IR region of the electromagnetic spectrum [8, 9]. In spite of these attractive properties, the commercial utilization of II–VI photodetectors has not reached its full potential yet. The main reason for this slow pace of commercialization is the difficulty in doping these materials. Most of the II–VI compounds exhibit a strong preference to either *p* or *n*-type conductivity [10–12]. Obtaining both types of conductivity in the same material has proved to be difficult. This limitation can be largely overcome by pairing two different II–VI materials in a heterojunction rather than trying to obtain *p*-*n* junction in the same material [11, 12]. Many heterojunctions based on II–VI materials are already in use [2, 13, 14]. The best example is the p-CdTe/n-CdS heterojunction which is being produced commercially as a thin film solar cell [15–18]. Devices based on ZnSe, ZnS, CdSe have also been studied for possible optoelectronic applications [2, 13–19].

The research work presented here makes use of a new technique of doping (namely Low melting point nanoparticle incorporation) to obtain bismuth (Bi) doped ZnTe films. This technique is highly effective in achieving uniform doping of thin films. In our previous publications [8, 20], we have compared the merits and demerits of this technique with those of conventional sandwiching technique. In this paper, we have used the said technique, for the first time, to fabricate a heterojunction device and have evaluated the characteristics of the heterojunction by comparing it with crystalline silicon based heterojunction. The study done here reveals that the Bi doped films obtained by nanoparticle incorporation can effectively be used in devices and they possess characteristics which are at-par with those that can be obtained in crystalline silicon based structures.

Both the heterojunctions (Bi:ZnTe/Al:ZnSe and Si/Al:ZnSe) fabricated and characterized in this research work are based on ZnSe thin films. In the first heterojunction, aluminium doped *n*-type ZnSe is paired with bismuth doped *p*-type zinc telluride (ZnTe). This structure has smaller lattice mismatch than the CdS/CdTe or ZnSe/CdTe structures reported in the past [21–25]. The second heterojunction uses commercially available *p*-type silicon substrates. The motivation behind the selection of this structure is the comparatively smaller lattice mismatch between silicon (5.43 ∀) and ZnSe (5.67 ∀).

✉ Gowrish K. Rao
kgowrishrao@gmail.com

[1] Department of Physics, Manipal Institute of Technology, Manipal University, Manipal, Udupi, Karnataka 576104, India

2 Experimental details

Deposition of thin films was performed inside a 12-inch vacuum chamber (HIND HIVAC) under a residual pressure less than 10^{-5} torr. ZnSe ingots (99.9% purity procured from Alfa Aesar) were evaporated in an electrically heated molybdenum boat to obtain ZnSe films. The same procedure was followed for ZnTe films. Well-cleaned glass substrates were used in all cases except for ZnSe–Si heterojunctions (where *p*-type Si substrates were used). Before the deposition, glass substrates were immersed first in chromic acid and then in acetone for 1 h each, rinsed in distilled water and dried. The native oxide layer on silicon substrates was removed by immersing them in dilute HF.

Vacuum evaporated ZnSe films are usually *n*-type [8, 9]. On the other hand, vacuum deposited ZnTe films are *p*-type [19]. However, the conductivity of these films is usually very low due to their nanocrystalline nature. Hence, in the present work, the conductivity of ZnTe and ZnSe films was enhanced by doping them with bismuth and aluminium, respectively. Bismuth doping was accomplished by nanoparticle incorporation technique discussed in our previous publications [8, 20]. The sandwiching technique was used to dope ZnSe films with aluminium [8].

To fabricate Bi:ZnTe/Al:ZnSe heterojunction, first a thin layer of bismuth nanoparticles was obtained on glass substrate kept at 453 K. Since bismuth is a low melting point material, a significant amount of re-evaporation takes place from the substrate maintained at 453 K [8, 20]. This re-evaporation prevents the formation of continuous films and produces a layer of bismuth nanoparticles. In the next cycle of deposition, ZnTe film (300 nm) was deposited on top of the bismuth nanoparticles. During this deposition the substrate was maintained at different elevated temperatures ranging from 300 to 423 K. Particles of ZnTe occupy the empty spaces between the bismuth particles and finally cover the whole layer of bismuth to form a continuous film. In our previous publication [20], we have shown that diffusion of bismuth into the semiconductor material takes place more efficiently when it is in nanoparticulate form. Elevated substrate temperature increases the surface mobility of the atoms and hence improves the crystallite size [8, 9, 19]. Besides, it also facilitates uniform diffusion of dopant atoms (bismuth) into the film. In the next step, ZnSe film (150 nm) was deposited on top of the ZnTe at different elevated substrate temperatures as mentioned above. Later, a very thin (nearly 50 nm) layer of aluminium (dopant) was deposited on top of the ZnSe layer, followed by another layer of ZnSe (150 nm) on top of it. Finally, silver contacts were thermally deposited on top of the structure using masks. The top silver contacts were in the form of stripes, with 3-mm gap in between them, to allow light to fall on the ZnSe layer. The schematic diagram of the heterojunction is shown in Fig. 1a.

Fabrication of Si/ZnSe heterojunction requires, comparatively, a lesser number of steps. In the first step, ZnSe film (150 nm) was deposited on crystalline *p*-type Si substrates (boron doped, resistivity:10^{-3} cm, procured from Sigma-Aldrich). The substrates were maintained at different temperatures ranging from 300 to 423 K. This was followed by deposition of a thin (50 nm) layer of aluminium and then a second layer of ZnSe (150 nm) on top of it. Finally, silver contacts were deposited on top. The schematic diagram of this structure is shown in Fig. 1b.

Electrical characterization of the heterojunctions was undertaken with the help of Keithley source meter (2400) and multimeter (2002). Wein-Kerr precision component analyzer was used for capacitance measurement. XRD analysis was performed using Rigaku minflex XRD unit. Photoresponse studies of the devices were carried out with the help of a precision monochromator and 150-W Xe arc lamp (spectral range of 200–2500 nm).

3 Results and discussion

Before the fabrication of heterojunctions, a detailed study of individual ZnSe and ZnTe films was performed separately. Details of this study can be found in our previous publications [9, 19]. Both ZnSe and ZnTe films were found to be polycrystalline. The average crystallite size of the films was determined from well-known Scherrer formula and the values thus obtained are given in Table 1. Since the fabrication of heterojunctions was done at different substrate temperatures, effect of substrate temperature on individual ZnSe and ZnTe films was also studied. It was found that the average crystallite size of both the films increases with the increase in substrate temperature (Table 1). Typical XRD patterns of the films are shown in Fig. 2.

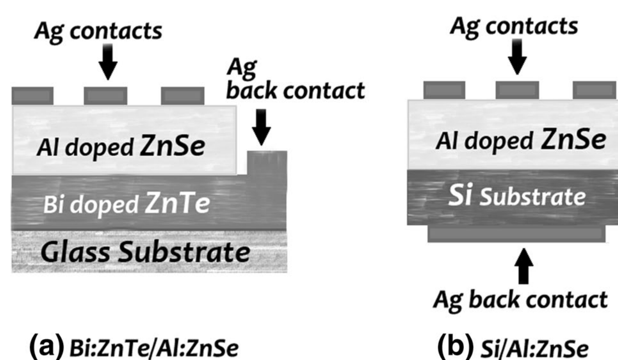

Fig. 1 Schematic diagram of the heterojunctions: **a** Bi:ZnTe/Al:ZnSe and **b** Si/Al:ZnSe (not according to scale)

Table 1 Structural and electrical properties of ZnSe and ZnTe films at different substrate temperatures

Film material	Substrate temperature (K)	Crystallite size (nm)	Composition (ratio Zn:X; where X is Se or Te)	Carrier density × 10^{14} (cm^{-3})		Mobility (cm^2/Vs)	
				Undoped	Doped	Undoped	Doped
ZnSe	300	55	0.90	4	39.8	16.1	8.7
	323	61	0.93	4	39.9	16.8	8.7
	343	67	0.95	4.1	40.3	17.1	9.7
	373	71	0.99	4.2	40.2	17.5	10.3
	423	76	1.0	4.3	40.4	20.5	12.9
ZnTe	300	38	0.87	2.9	28	16.3	7.2
	323	40	0.88	3	29.1	15.9	7.4
	343	42	0.88	3	30.2	16	7.1
	373	46	0.93	3.2	31.3	15	7.7
	423	49	0.95	3.6	32.2	15.5	7.4

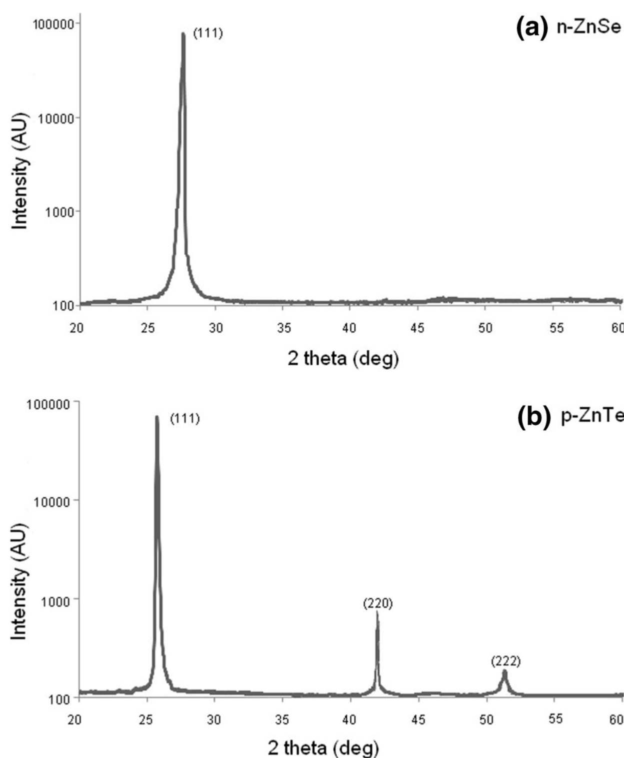

Fig. 2 Typical XRD patterns of doped films: **a** ZnSe and **b** ZnTe

The composition of the films was determined by EDAX analysis. The composition of vacuum deposited films usually deviates from that of the source material because of the difference in vapor pressures of constituent elements [9, 19]. In the present case, room temperature deposited ZnSe and ZnTe films were found to be slightly rich in selenium (Zn:Se ratio of 0.9) and tellurium (Zn:Te ratio of 0.9), respectively. This small offset in stoichiometry reduced at higher substrate temperatures due to the evaporation of excess selenium (in ZnSe) or tellurium (in ZnTe) content. Films obtained at higher substrate temperatures were stoichiometric.

Optical absorbance spectra of the individual films (Fig. 3a) were studied to probe their band structure. Both ZnTe and ZnSe are direct bandgap materials which show steep increase in absorbance for photon having energy higher than their bandgap. The bandgap of ZnTe and ZnSe films were estimated from Tauc plots illustrated in Fig. 3b. The values thus obtained were close to 2.25 and 2.7 eV, respectively, for ZnTe and ZnSe films.

The carrier density and mobility of the individual films were determined by Hall effect analysis using van der Paw technique [26]. The results of the analysis are given in Table 1. Incorporation of bismuth particles enhanced the hole concentration of ZnTe films by nine times. On the other hand, free electron concentration of ZnSe films increased almost ten times after aluminium doping (Fig. 4).

3.1 Dark current characteristics

Dark current vs voltage (I–V) curves of Bi:ZnTe/Al:ZnSe and Si/Al:ZnSe heterojunctions are shown in Fig. 4 for different substrate temperatures. The rectifying behavior of the heterojunctions is clearly visible. The rectification ratios of Bi:ZnTe/Al:ZnSe and Si/Al:ZnSe heterojunctions were found to be about 280 and 300, respectively. The electrical conduction in the heterojunctions can be explained by Sze and Crowell model [27]. This model attributes the electrical conduction in heterojunctions to thermionic emission and diffusion. The forward current through the junction is related to voltage by the equation:

$$I = AA^{*}T^{2}\exp\left(\frac{-\phi}{kT}\right)\exp\left(\frac{qV}{nkT}\right), \quad (1)$$

where A is the the area of the device, A^* is the Richardson constant, ϕ is the barrier height, k is the Boltzmann's

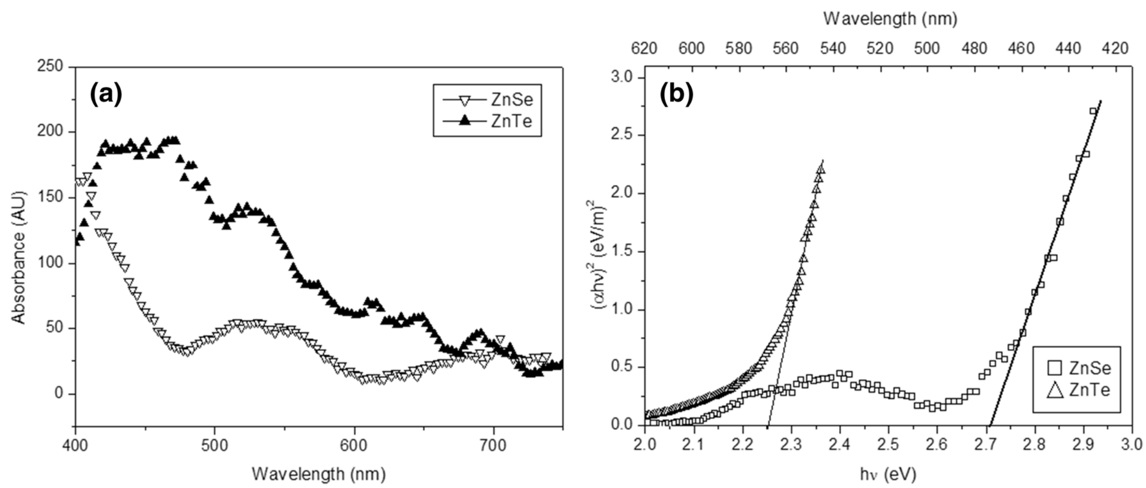

Fig. 3 **a** Typical absorbance spectra and **b** Tauc plots of doped ZnSe and ZnTe films

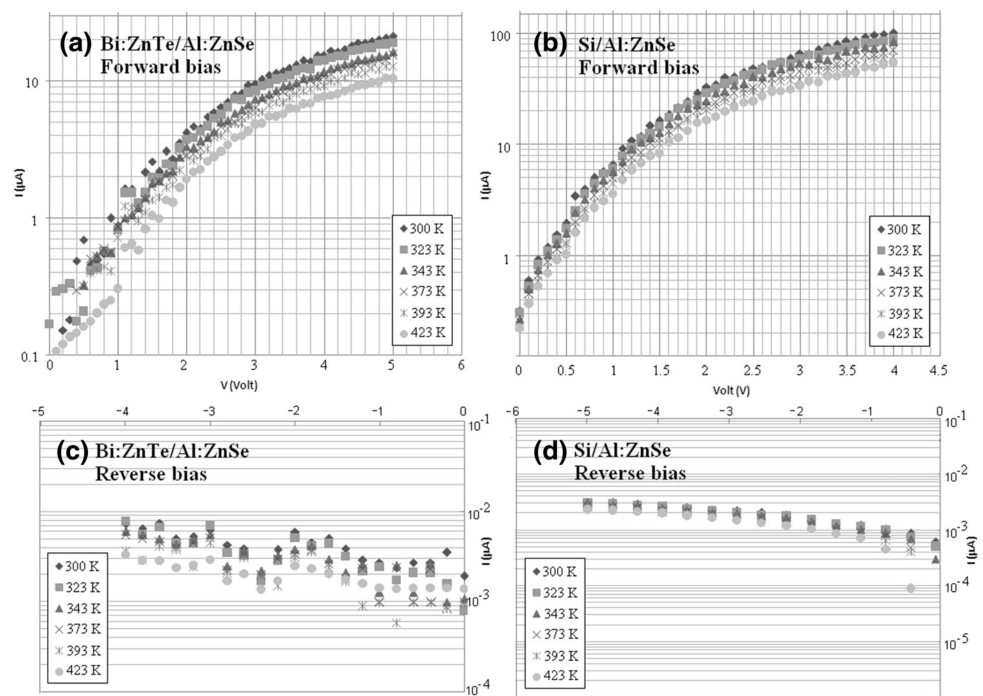

Fig. 4 I–V characteristic curves of the heterojunctions at various substrate temperatures. Bi:ZnTe/Al:ZnSe: (**a**) and (**c**), Si/Al:ZnSe: (**b**) and (**d**)

constant, n is the diode ideality factor, T is the temperature and q is the elementary charge.

Since reverse saturation current I_s is given by [27],

$$I_s = AA^*T^2 \exp\left(\frac{-\phi}{kT}\right). \tag{2}$$

Equation (1) can be re-written as:

$$I = I_s \exp\left(\frac{qV}{nkT}\right). \tag{3}$$

In the present case, the variation of ln (I) with V (Fig. 5) was found to be linear in both the heterojunctions, which suggests that the thermionic emission is the dominant conduction mechanism at low bias voltages. The diode ideality factor ‘n’ was found to be about 3.9 and 3.6, respectively, for Bi:ZnTe/Al:ZnSe and Si/Al:ZnSe heterojunctions. Such high values are usually expected in thin film based devices due to the fine grain structure of the films [26–28]. When compared to films obtained by high-end techniques such as molecular beam epitaxy, the vacuum deposited films have much less grain size and therefore large grain boundary regions. Defects arising in the grain boundary regions limit the flow of free charges by acting as carrier traps.

Typical thermionic emission is also characterized by a linear relation between ln (I_s/T^2) and $1/T$ as shown in Eq. (2). In the present case, ln (I_s/T^2) was actually found to vary linearly with $1/T$ as shown in Fig. 5. This observation further proves that the conduction mechanism operating in both the heterojunctions is thermionic emission. The barrier heights (determined from slope of the graph in Fig. 6) were found to be 0.85 and 0.74 eV for Bi:ZnTe/Al:ZnSe and Si/Al:ZnSe heterojunctions, respectively.

The junction capacitance of the heterostructures was measured using Schottky relation [28]:

$$\frac{1}{C^2} = 2\left[\frac{\left(V - V_b + \frac{kT}{q}\right)}{q\varepsilon_0\varepsilon_r N A^2}\right], \tag{4}$$

where V is the applied reverse bias voltage, V_b is the diffusion potential, N is the space charge density and A is the effective area of the diode. Figure 7 shows the variation of C^{-2} with reverse bias voltage (recorded at a frequency of 300 kHz) for Bi:ZnTe/Al:ZnSe and Si/Al:ZnSe heterojunctions. The graph shows a linear variation of C^{-2} with reverse voltage V, in accordance with the Eq. (4). This indicates that the carrier concentration is uniform and the junction is an abrupt junction. The value of N was determined from the slope of the graph using the Eq. [28],

$$\frac{dC^{-2}}{dV} = \frac{2}{q\varepsilon_0\varepsilon_r N A^2}. \tag{5}$$

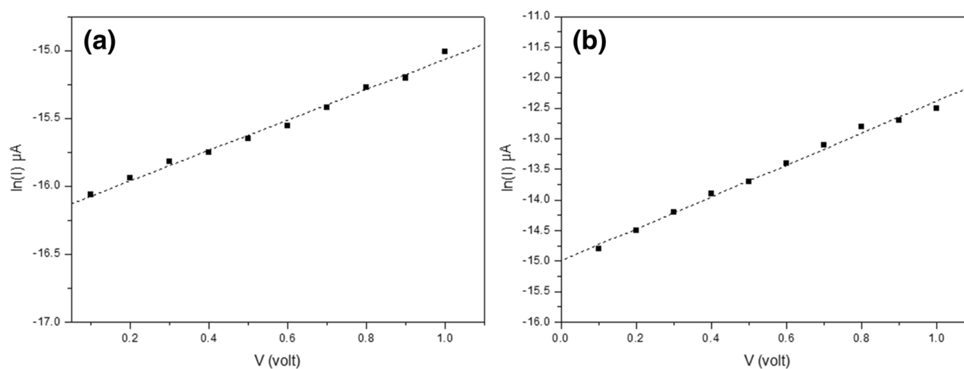

Fig. 5 ln (I) vs V plots of **a** Bi:ZnTe/Al:ZnSe and **b** Si/Al:ZnSe heterojunctions

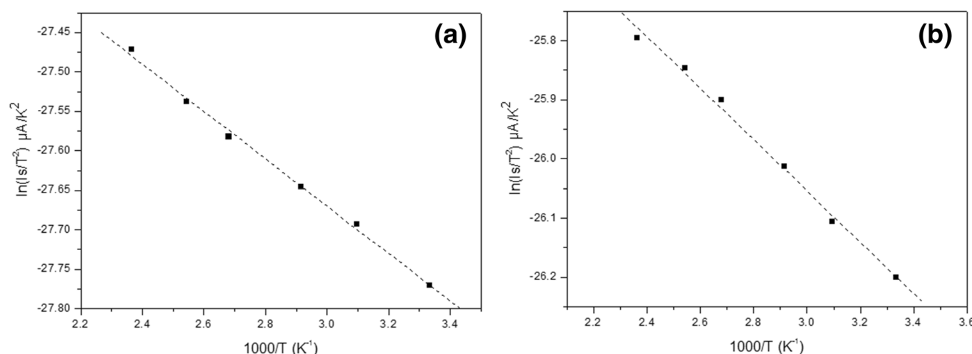

Fig. 6 Variation of ln (I_s/T^2) with $1/T$ in **a** Bi:ZnTe/Al:ZnSe and **b** Si/Al:ZnSe heterojunctions

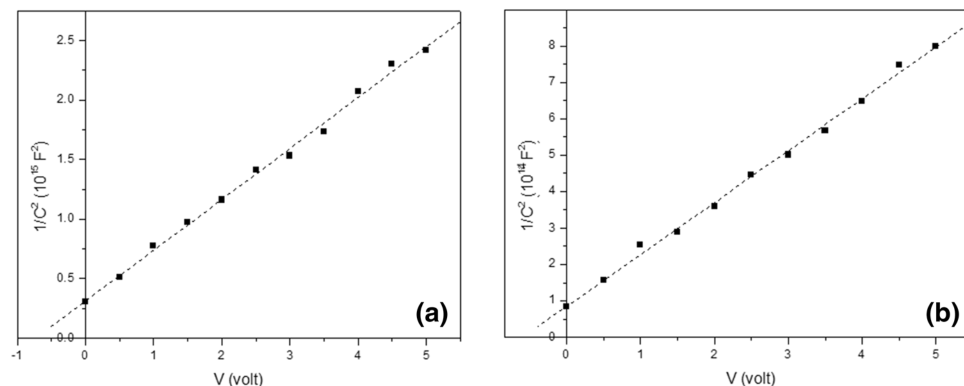

Fig. 7 Variation of $1/C^2$ with V in **a** Bi:ZnTe/Al:ZnSe and **b** Si/Al:ZnSe heterojunctions

The values thus obtained were found to be about 2.12×10^{19} $m^{-3}$and 8×10^{19} m^{-3}, respectively, for Bi:ZnTe/Al:ZnSe and Si/Al:ZnSe heterojunctions. The thickness d_s of the depletion region is given by the equation,

$$d_s = \frac{\varepsilon_0\varepsilon_r A}{C_0}, \quad (6)$$

where C_0 is the capacitance at zero bias. In the present case, the observed values of d_s were about 25 nm for Bi:ZnTe/Al:ZnSe and 13.5 nm for Si/Al:ZnSe heterojunction.

3.2 Photoresponse studies

Normalized spectral response curves of the two heterojunctions are shown in Fig. 8. In both cases, a large peak was observed at around 455 nm which corresponds to photon energy of about 2.7 eV. This peak is resulting from photon absorption in ZnSe layer. A second smaller peak is also visible in the case of Bi:ZnTe/Al:ZnSe heterojunction at around 550 nm. This secondary peak corresponds to energy bandgap of ZnTe (2.5 eV). There is no visible secondary peak in Si/Al:ZnSe heterojunction as Si has absorption edge in infrared region (above 800 nm). Because of the narrow bandgap of silicon, Si/Al:ZnSe heterojunction exhibits considerably higher amount of photocurrent in longer wavelength (455 to 800 nm) region than Bi:ZnTe/Al:ZnSe heterojunction. In both the heterojunctions, light first falls on ZnSe layer where only wavelengths below 455 nm are absorbed and rest of the wavelengths are either reflected or transmitted towards the *p*-type layer. The *p*-type layers only absorb photons which have wavelengths below the one corresponding to their bandgap.

I–V characteristics of the heterojunctions under illumination are shown in Figs. 10a and 11a. The current $I'$and the applied voltage follow the relation [27]:

$$I' = I'_S \exp\left(\frac{qV}{n'kT}\right), \quad (7)$$

where I'_S is the reverse saturation current under illumination and n' is the diode ideality factor under illumination. The values of I'_S and n' obtained in the present case are given in Table 2. In both the heterojunctions; the short-circuit current under illumination increases with the increase in substrate temperature (Fig. 9a, b). This increase can be attributed to the improved crystallite size of the films obtained at higher substrate temperature. The photoconduction mechanism in nanocrystalline films can be explained by the models proposed by Slater and Petritz [29, 30]. According to this model, photoconduction in thin films is due to the combined effect of increase in the number of free charge carriers ρ and increased effective carrier mobility μ^*. The change in conductivity $\Delta\sigma$ is therefore given by,

$$\Delta\sigma = q\rho\Delta\mu^* + q\mu^*\Delta\rho, \quad (8)$$

where μ^* and $\Delta\mu$ are given by [24, 25],

$$\mu^* = \mu \exp\left(-\frac{q\phi}{kT}\right), \quad (9)$$

$$\Delta\mu^* = -\frac{q\mu}{kT} \exp\left(-\frac{q\phi}{kT}\right)\Delta\phi. \quad (10)$$

Here $\Delta\phi$ denotes the change in barrier height due to illumination. Although the primary effect of illumination is the generation of free charge carriers, the lowering of inter-grain barrier height also contributes to the overall photoconduction.

The speed of photoresponse of the heterojunctions was studied by illuminating the junctions with pulsating light. A variable frequency optical chopper was attached to the Xe arc source to obtain pulsating light. A digital storage oscilloscope was used to record the rise and decay of photo-voltage. As with most of the thin film photodetectors, the rise of photo-voltage in both the heterojunctions was found to be much faster than the decay (Fig. 10). In our previous publications [9, 26], we have reported such behavior in the photoresponse of individual thin films as well. The decay of photo-voltage is relatively slow due to the presence of carrier traps. The decay process follows the exponential relation [27]:

$$V(t) = V_0 \exp(-pt), \quad (11)$$

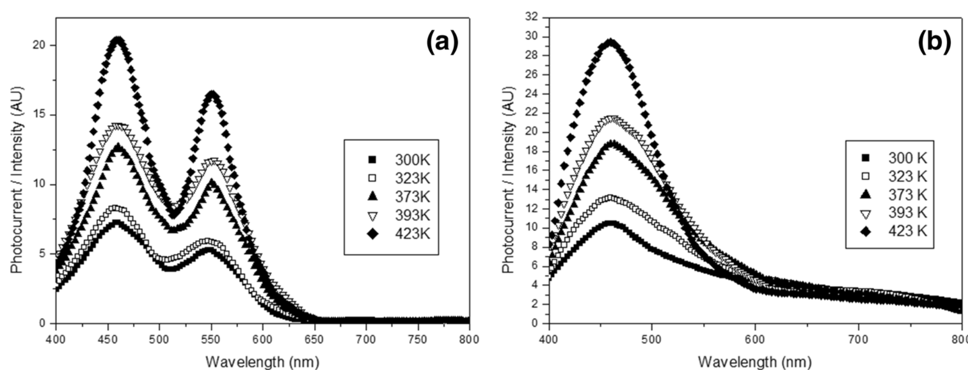

Fig. 8 Normalized spectral response curves of **a** Bi:ZnTe/Al:ZnSe and **b** Si/Al:ZnSe heterojunctions at various substrate temperatures

Table 2 Photoresponse properties of the heterojunctions

Heterojunction	Substrate temperature (K)	Short-circuit current under illumination $I'_{sc}(\mu A)$	Ideality factor under illumination′	Speed of photoresponse	
				Rise time (μs)	Decay time (μs)
Bi:ZnTe/Al:ZnSe	300	0.58	3.1	7	51
	323	0.89	2.9	6	48
	343	1.46	2.9	6	45
	373	1.78	2.8	6	41
	393	2.24	2.8	6	38
	423	2.87	2.7	6	35
Si/Al:ZnSe	300	0.79	3.0	7	43
	323	1.48	2.8	6	40
	343	1.85	2.8	6	37
	373	2.45	2.7	6	33
	393	2.90	2.7	6	31
	423	3.49	2.6	6	29

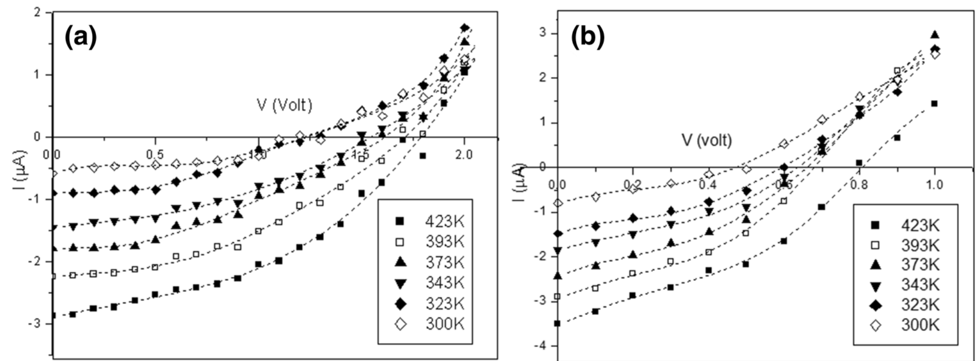

Fig. 9 Short-circuit current (I_{sc}) in **a** Bi:ZnTe/Al:ZnSe and **b** Si/Al:ZnSe heterojunctions under illumination (at different substrate temperatures)

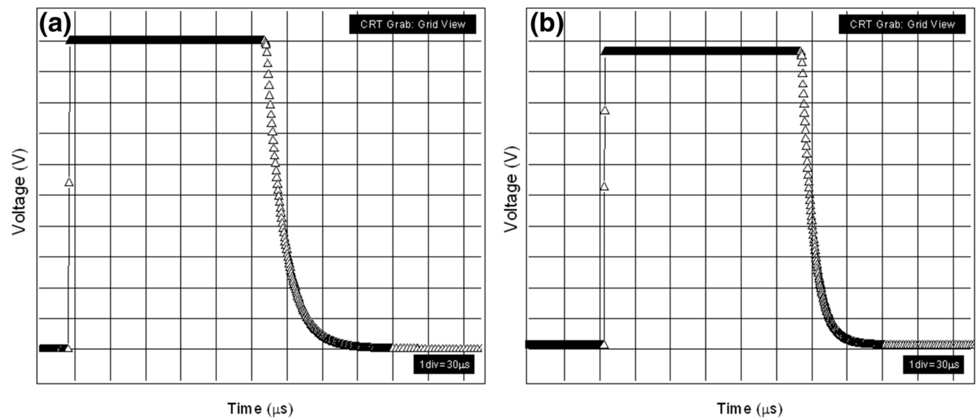

Fig. 10 Photoresponse of **a** Bi:ZnTe/Al:ZnSe and **b** Si/Al:ZnSe heterojunctions.(*Y axis* shows voltage drop due to photocurrent)

where p is the probability of escape of an electron from a trap per second. Typically, this probability is given by [27],

$$p = f\left[\exp\left(-\frac{E_{tr}}{kT}\right)\right], \tag{12}$$

where f is the frequency factor ($\cong 10^{10}$ s^{-1}) and E_{tr} is the trap depth. The values of trap depth obtained in the present case were in the range of 0.30–0.32 eV for Bi: ZnTe/Al:ZnSe and 0.27–0.29 eV for Si/Al:ZnSe heterojunctions, respectively. Decay time of both the heterojunctions

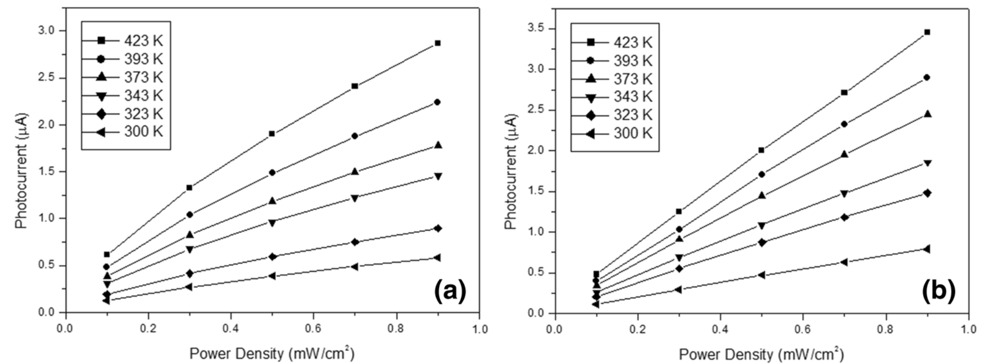

Fig. 11 Variation of photocurrent with light power density in **a** Bi:ZnTe/Al:ZnSe and **b** Si/Al:ZnSe heterojunctions (at different substrate temperatures and at 450 nm wavelength)

reduced with the increase in substrate temperature. This improvement can be attributed to the enhanced crystallite size of the films deposited at higher substrate temperatures. The larger crystallite size means lesser grain boundary regions which facilitate faster response [28].

The photocurrent I in a typical thin film photodiode varies with light power density P according to the relation [28],

$$I \infty P^k, \tag{13}$$

where k is some constant. In the present case, the variation of I with P was found to be sub-linear ($k<1$) for Bi:ZnTe/Al:ZnSe; and almost linear ($k=1$) for Si/Al:ZnSe heterojunction as shown in Fig. 11. The sub-linear variation in Bi:ZnTe/Al:ZnSe heterojunction results from the exponential distribution of carrier traps in the band gap [32, 33]. As intensity of the radiation increases, increasing number of traps are converted into recombination centers; thereby shifting the quasi-Fermi level towards the edge of the conduction band. This behavior has been observed in individual thin films as well [9, 31]. In Bi:ZnTe/Al:ZnSe heterojunction, the effect is predominant since both p and n regions are nanocrystalline thin films. On the other hand; in Si/Al:ZnSe heterojunction, the sub-linear nature of ZnSe is overshadowed by the far superior crystallinity of silicon which has relatively high carrier density.

4 Conclusions

Bi:ZnTe/Al:ZnSe and Si/Al:ZnSe thin film photodiodes were fabricated by thermal evaporation process. Both devices showed maximum photoresponse at 455 nm which corresponds to energy bandgap of ZnSe layer. Photon absorption in the *p*-type layer was also found to contribute to the observed photocurrent. Bi:ZnTe/Al:ZnSe device offers better contrast in short wavelength region when compared to Si/Al:ZnSe. The latter produces considerable amount of photocurrent in longer wavelength region due to the narrow bandgap of silicon. The rise of photocurrent with intensity was found to be slightly sub-linear in Bi:ZnTe/Al:ZnSe while Si/Al:ZnSe showed almost linear increase in photocurrent. Si/Al:ZnSe device was also found to have faster response time partly due to better lattice matching between the two layers and also due to superior crystalline properties of silicon layer.

References

1. A.A. Ibrahim, N.Z. El-Sayed, M.A. Kaid, A. Ashour, Vacuum **75**, 189 (2004)
2. K.P. Acharya, A. Erlacher, B. Ullrich. Thin Solid Films **515**, 4066 (2007)
3. Q. Guo, Y. Kume, Y. Fukuhara, T. Tanaka, M. Nishio, H. Ogawa, M. Hiratsuka, M. Tani, M. Hangyo. Solid State Commun. **141**, 188 (2007)
4. C.X. Shan, X.W. Fan, J.Y. Zhang, Z.Z. Zhang, X.H. Wang, J.G. Ma, Y.M. Lu, Y.C. Liu, D.Z. Shen, X.G. Kong, G.Z. Zhong, J. Vac. Sci. Technol. **20**, 1886 (2002)
5. K. Yoshino, A. Memon, M. Yoneta, K. Ohmori, H. Sato, M. Ohishi, Phys. Status Solidi **229**, 977 (2002)
6. A. Ueta, D. Hommel, Phys. Status Solidi **192**, 177 (2002)
7. J.H. Chang, T. Takai, K. Godo, J.S. Song, B.H. Koo, T. Hanada, Phys. Status Solidi **229**, 995 (2002)
8. G.K. Rao, Mater. Sci. Semicond. Process, **26**, 137–143 (2014)
9. G.K. Rao, K.V. Bangera, G.K. Shivakumar, Solid State Sci. **13**, 1921–1925 (2011)
10. U.V. Desnica, Prog. Cryst. Growth Charact, **36**, 291–357 (1998)
11. D.J. Chadi, Phys. Rev. Lett. **72**, 534–536 (1994)
12. D.J. Chadi, Mater. Sci. Semicond. Process. **6**, 281–284 (2003)
13. G.K. Rao, K.V. Bangera, G.K. Shivakumar, Solid State Electron **56**, 100–103 (2011)
14. G.K. Rao, K.V. Bangera, G.K. Shivakumar, Solid State Electron **54**, 787–790 (2010)
15. X. Mathew, Semicond. Sci. Technol. **18**, 1–4 (2003)
16. N. Romeo, A. Bosio, V. Canevari, A. Podestà, Sol. Energy **77**, 795–801 (2004)
17. N. Romeo, A. Bosio, R. Tedeschi, A. Romeo, V. Canevari, Sol. Energy Mater. Sol. Cells **58**, 209–218 (1999)
18. H.A. Mohamed, J. Appl. Phys. **113**, 093105 (2013)
19. G.K. Rao, K.V. Bangera, G.K. Shivakumar, Vacuum, **83**, 1485–1488 (2009)
20. G.K. Rao, G.K. Shivakumar, K.V. Bangera, Mater. Sci. Eng. B, **175**, 185–188 (2010)
21. Z. Fang, X.C. Wang, H.C. Wu, C.Z. Zhao, Int. J. Photoenergy **2011**, (2011)

22. S.S. Babkair, JKAU Sci. **22**, 21–33 (2010)
23. R.G. Dhere, Y. Zhang, M.J. Romero, S.E. Asher, M. Young, B. To, R. Noufi, T.A. Gessert, 33rd IEEE Photovoltaic Specialists Conference San Diego, California (2008) 1–5
24. T.L. Chu, S.S. Chu, S.T. Ang, J. Appl. Phys. **64**, 1233 (1988)
25. T. Gaewdang, N. Wongcharoen, T. Wongcharoen, Energy Proc. **15**, 299–304 (2012)
26. L.J. Van der Pauw, Philips Technic. Rev. **20**, 220–224 (1958)
27. C. Lamberti, Characterization of Semiconductor Heterostructures and Nanostructures. Elsevier Publication; (2008)
29. E.H. Rhoderick, R.H. Williams, Metal semiconductor contacts. Oxford Science Publications; (1988)
30. J.C. Slater, Phys. Rev. **103**, 1631 (1956)
31. R.L. Petritz, Phys. Rev. **104**, 1509 (1956)
32. G.K. Rao, K.V. Bangera, G.K. Shivakumar. Mater. Res. Bull. **45**, 1357–1360 (2010)
33. M. Buragohain, K. Barua, Thin Solid Films **99**, L1 (1983)
34. N.V. Joshi, Photoconductivity: Art, Science and Technology, Marcel Dekker Inc.(1990) 95.